

Electronic Supporting Information

Experimental and theoretical magnetostructural study on discrete heterometallic cyanide-bridged dinuclear Fe^{III}Mn^{II} and tetranuclear Fe^{III}₂Cu^{II}₂ complexes bearing a tripodal pyrazolyl borate and tetradentate phenolate-based ligands

Akhilesh Kumar^{a,c,#}, Amit Rajput^{b,#}, Pawanjeet Kaur^d, Indresh Verma^a, Rohan D. Erande^e, Saleem Javed^f, Julia Kłak^{*,g}, Shefa' F. Alrebei^h, Antonio J. Mota^{*,h}, Enrique Colacio^{*,h}, and Himanshu Arora^{*,d,i}

^aDepartment of Chemistry, Indian Institute of Technology Kanpur, Kanpur 208016, India.

^bDepartment of Chemistry, J. C. Bose University of Science & Technology, YMCA, Faridabad 121006, India.

^cDepartment of Chemistry and Nano Science, Ewha Womans University, Seoul 03760, Korea.

^dSchool of Engineering and Sciences, G.D. Goenka University, Gurugram, India. E-mail: himanshuiitk2004@gmail.com, +91 8860185079.

^eDepartment of Chemistry, Indian Institute of Technology Jodhpur, Jodhpur 342037, India.

^fDepartment of Chemistry, Faculty of Natural Science, Jamia Milia Islamia, Delhi 110025, India

^gFaculty of Chemistry, University of Wrocław, Wrocław 50-383, Poland.

^hDepartment of Inorganic Chemistry, Faculty of Science, University of Granada, 18071, Granada, Spain.

ⁱDepartment of Chemistry, Faculty of Science, Central University of Allahabad, Prayagraj, Uttar Pradesh 211002, India

#Both the authors have equal contribution.

1. Schematic drawing of 1-2	Figs. S1-S2
2. CShM values for the octahedral coordination around the metal center appearing in complexes 1 and 2	Fig. S3
3. IR of 1-2	Figs. S4-S5
4. UV-Vis of 1-2 in DMF	Figs. S6-S7
5. Crystallographic data	Table S1, S3

6. Bond Valence Calculation

7. Magnetic study

8. Calculated LC- ω PBE/TZVP spin density for 1 & 2

9. DFT study

Table S2

Figs. S8-S11

Figs. S12-S13

Tables **S4-S5**

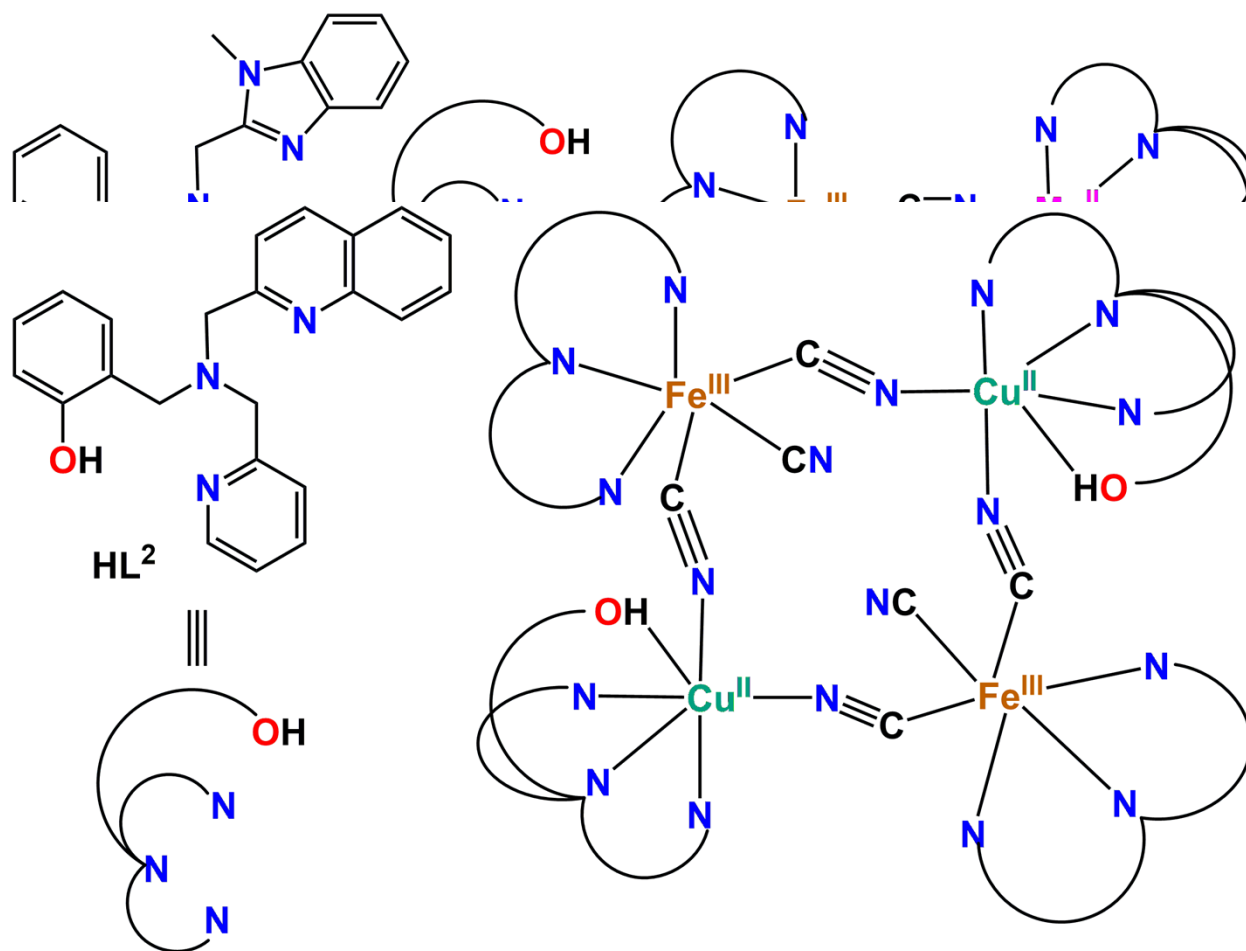


Figure S1. Schematic representation of metal coordination environment in the cluster $[\text{Fe}^{\text{III}}(\text{Tp})(\text{CN})_2(\mu\text{-CN})\text{Mn}^{\text{II}}\text{Cl}(\text{HL}^1)] \cdot 3\text{DMF}$ (**1**), along with the ligand employed in this study.

Figure S2. Schematic representation of metal coordination environment in the cluster $\{[\text{Fe}^{\text{III}}(\text{Tp})(\text{CN})(\mu_2\text{-NC})_2\text{Cu}^{\text{II}}(\text{HL}^2)](\text{ClO}_4)\}_2 \cdot 6\text{DMF}$ (**2**), along with the ligand employed in this study.

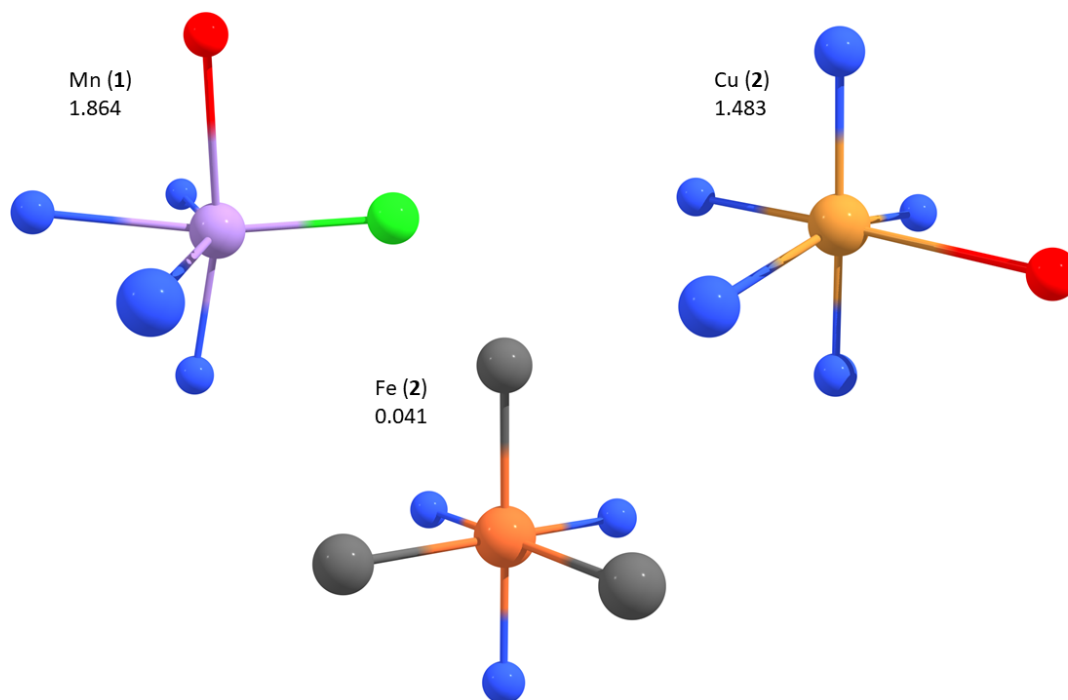


Figure S3. CShM values for the octahedral coordination around the metal center appearing in complexes 1 and 2. Only iron present in complex 2 is shown as example.

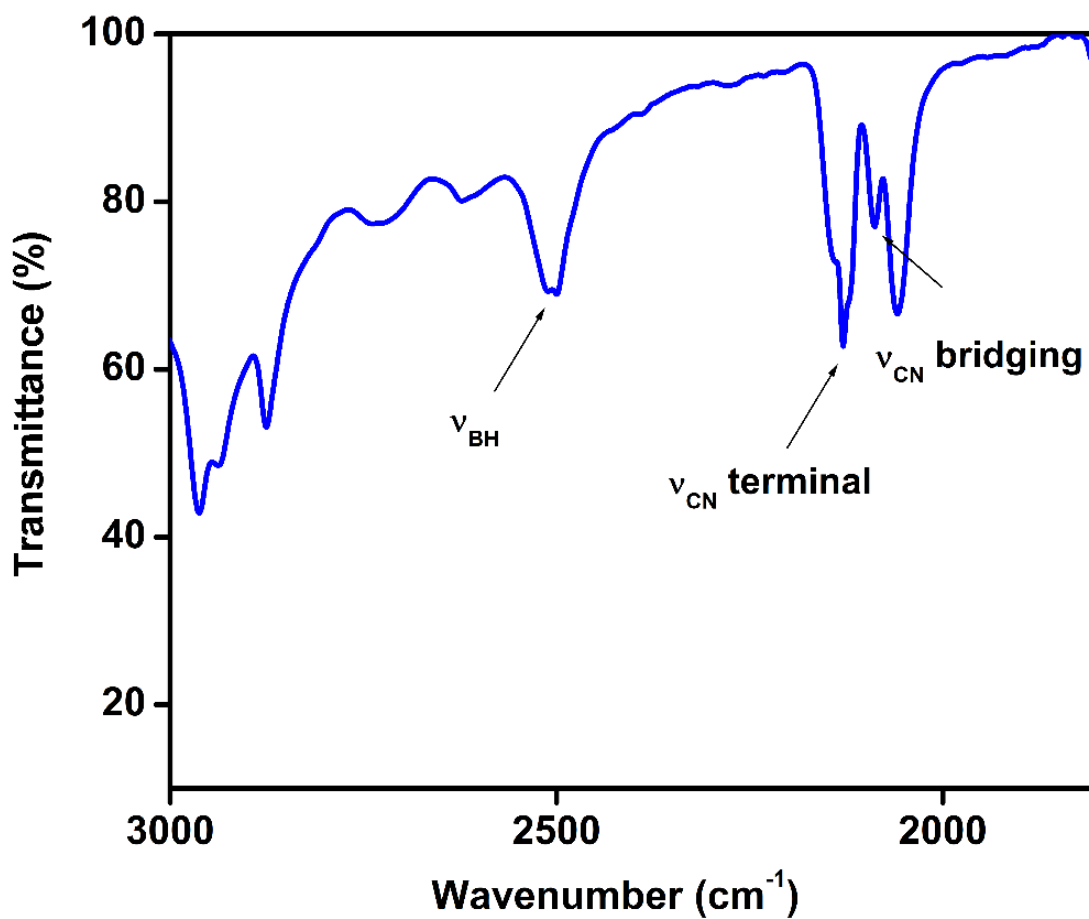


Figure S4. Selected portion of IR spectra (in KBr) of **1**.

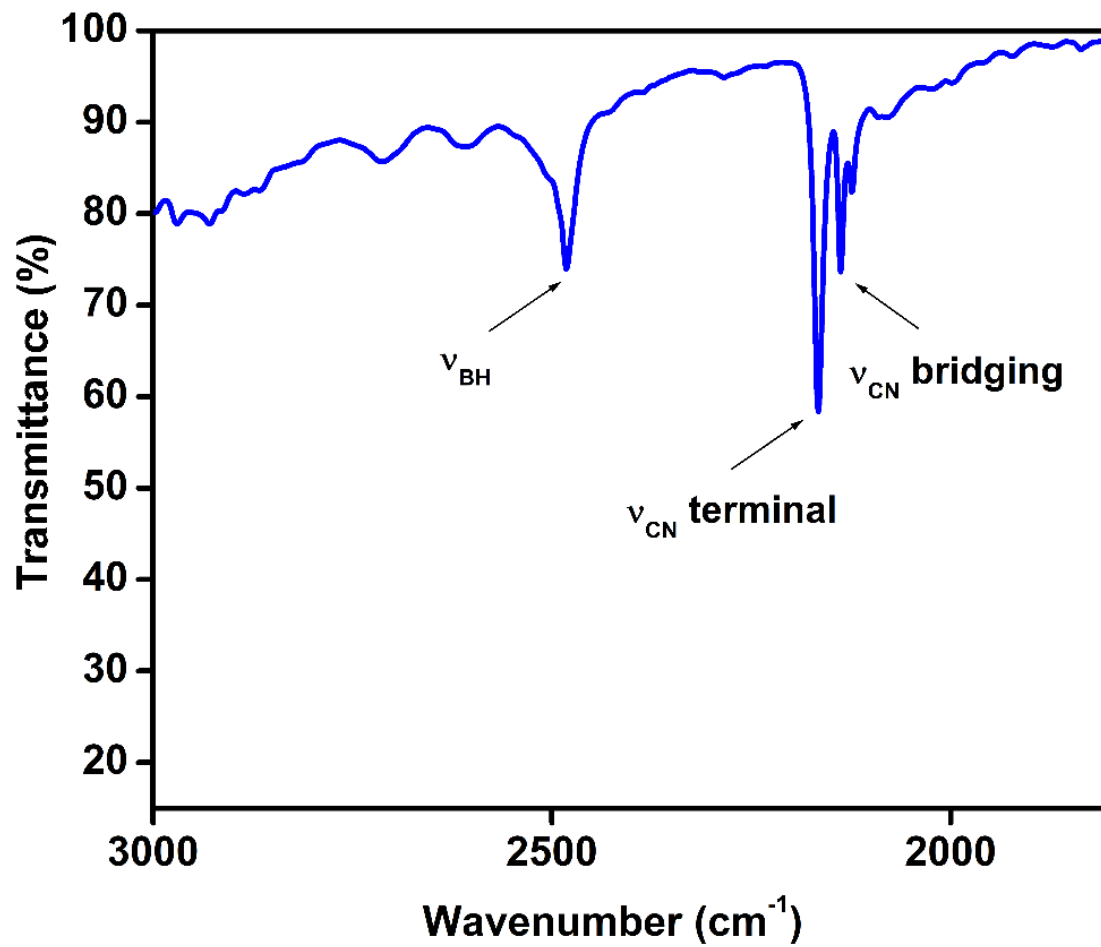


Figure S5. Selected portion of IR spectra (in KBr) of 2.

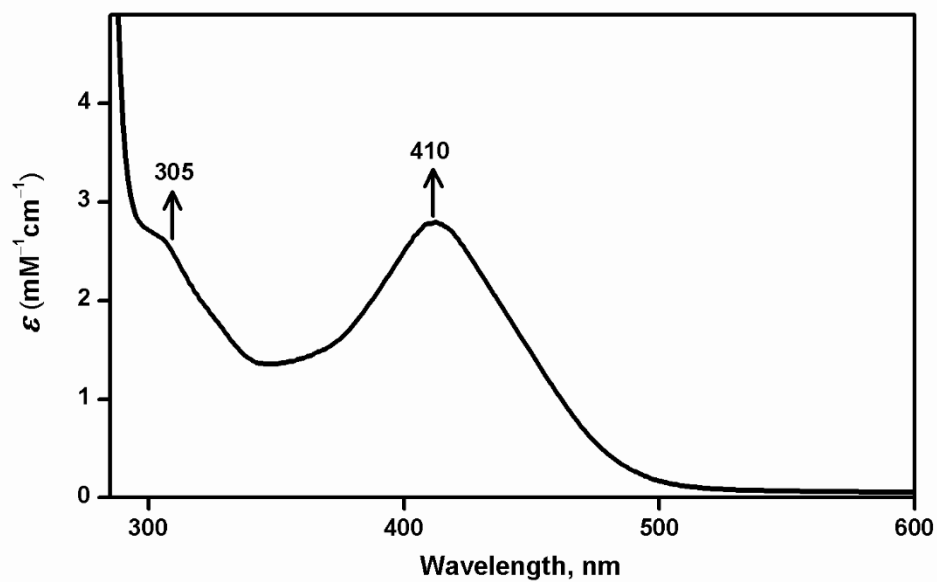


Figure S6. Electronic spectra in DMF of **1**.

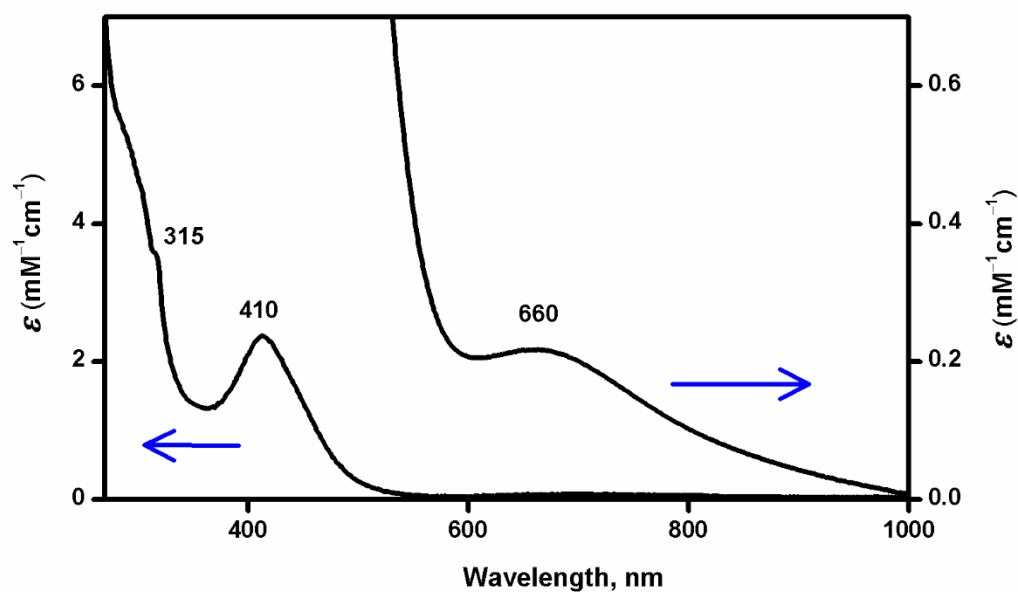


Figure S7. Electronic spectra in DMF of **2**.

Crystallographic data

Table S1. Selected bond angles [$^\circ$] of $[\text{Fe}^{\text{III}}(\text{Tp})(\text{CN})_2(\mu\text{-CN})\text{Mn}^{\text{II}}\text{Cl}(\text{HL}^1)] \cdot 3\text{DMF}$ (**1**) and $\{[\text{Fe}^{\text{III}}(\text{Tp})(\text{CN})(\mu_2\text{-NC})_2\text{Cu}^{\text{II}}(\text{HL}^2)](\text{ClO}_4)\}_2 \cdot 6\text{DMF}$ (**2**).



C(1)–Fe(1)–C(2)	86.85(17)	C(1)–Fe(1)–C(3)	87.25(17)
C(2)–Fe(1)–C(3)	87.87(18)	C(1)–Fe(1)–N(8)	93.18(16)
C(1)–Fe(1)–N(10)	93.27(16)	C(1)–Fe(1)–N(12)	177.28(17)
C(2)–Fe(1)–N(8)	92.60(17)	C(2)–Fe(1)–N(10)	179.8(2)
C(2)–Fe(1)–N(12)	91.90(16)	C(3)–Fe(1)–N(8)	179.38(16)
C(3)–Fe(1)–N(10)	91.96(16)	C(3)–Fe(1)–N(12)	90.29(16)
N(8)–Fe(1)–N(10)	87.56(15)	N(8)–Fe(1)–N(12)	89.29(14)
N(10)–Fe(1)–N(12)	87.98(14)	Fe(1)–C(1)–N(1)	178.6(4)
Fe(1)–C(2)–N(2)	178.5(4)	Fe(1)–C(3)–N(3)	179.0(4)
N(1)–Mn(1)–O(1)	167.23(12)	N(1)–Mn(1)–N(4)	86.45(12)
N(1)–Mn(1)–N(6)	88.22(12)	N(1)–Mn(1)–N(7)	91.36(13)
N(1)–Mn(1)–Cl(1)	101.39(10)	N(4)–Mn(1)–O(1)	95.07(12)
N(4)–Mn(1)–N(6)	74.21(13)	N(4)–Mn(1)–N(7)	148.13(14)
N(4)–Mn(1)–Cl(1)	104.43(11)	N(6)–Mn(1)–O(1)	80.04(11)
N(6)–Mn(1)–N(7)	73.95(13)	N(6)–Mn(1)–Cl(1)	170.24(9)
N(7)–Mn(1)–O(1)	80.64(12)	N(7)–Mn(1)–Cl(1)	107.16(10)
Cl(1)–Mn(1)–O(1)	90.53(8)	C(1)–N(1)–Mn(1)	163.9(3)

$\{[\text{Fe}^{\text{III}}(\text{Tp})(\text{CN})(\mu_2\text{-NC})_2\text{Cu}^{\text{II}}(\text{HL}^2)](\text{ClO}_4)\}_2 \cdot 6\text{DMF}$			
C(1)–Fe(1)–C(2)	88.33(15)	C(1)–Fe(1)–C(3)	90.80(15)
C(2)–Fe(1)–C(3)	89.40(15)	C(1)–Fe(1)–N(4)	90.69(13)
C(1)–Fe(1)–N(6)	89.34(14)	C(1)–Fe(1)–N(9)	177.92(14)

C(2)–Fe(1)–N(4)	178.98(14)	C(2)–Fe(1)–N(6)	91.74(14)
C(2)–Fe(1)–N(9)	92.56(14)	C(3)–Fe(1)–N(4)	90.34(13)
C(3)–Fe(1)–N(6)	178.86(14)	C(3)–Fe(1)–N(9)	91.09(14)
N(4)–Fe(1)–N(6)	88.52(12)	N(4)–Fe(1)–N(9)	88.43(12)
N(6)–Fe(1)–N(9)	88.75(13)	Fe(1)–C(1)–N(1)	171.1(3)
Fe(1)–C(3)–N(2)	176.3(3)	Fe(1)–C(2)–N(3)	177.9(3)
N(1)–Cu(1)–O(1)	93.99(11)	N(1)–Cu(1)–N(10)	95.05(12)
N(1)–Cu(1)–N(11)	176.18(13)	N(1)–Cu(1)–N(12)	101.36(13)
N(10)–Cu(1)–O(1)	87.84(11)	N(10)–Cu(1)–N(11)	82.70(12)
N(10)–Cu(1)–N(12)	163.60(12)	N(11)–Cu(1)–O(1)	89.01(11)
N(11)–Cu(1)–N(12)	80.91(12)	N(12)–Cu(1)–O(1)	91.24(11)
C(1)–N(1)–Cu(1)	161.2(3)		

Magnetic study

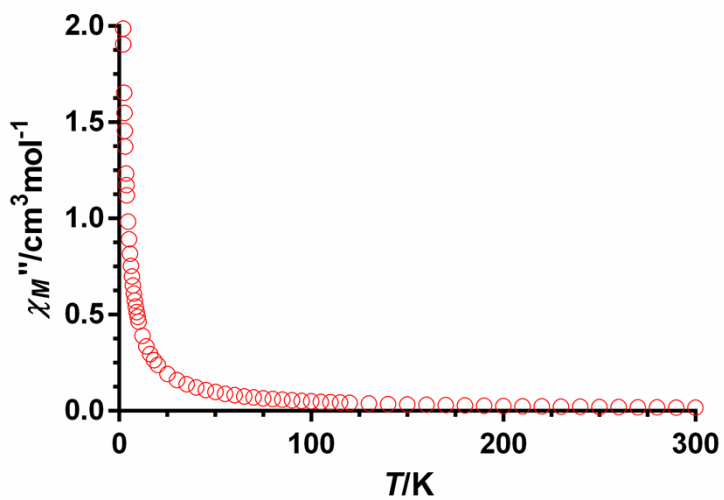


Figure S8. Temperature dependence of the χ_M for **1**.

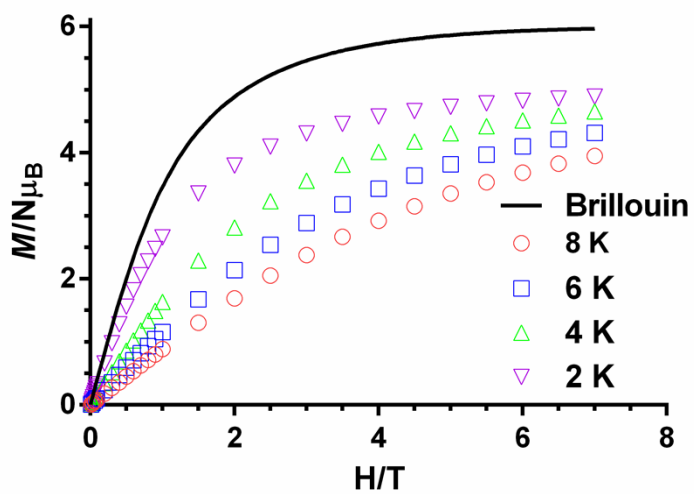


Figure S9. Field dependence of the magnetization for **1** at different temperatures (2–8 K). The solid black line represent the Brillouin function curve for non-interacting Mn ($S = 5/2$) and Fe ($S = 1/2$) ions with $g = 2.0$.

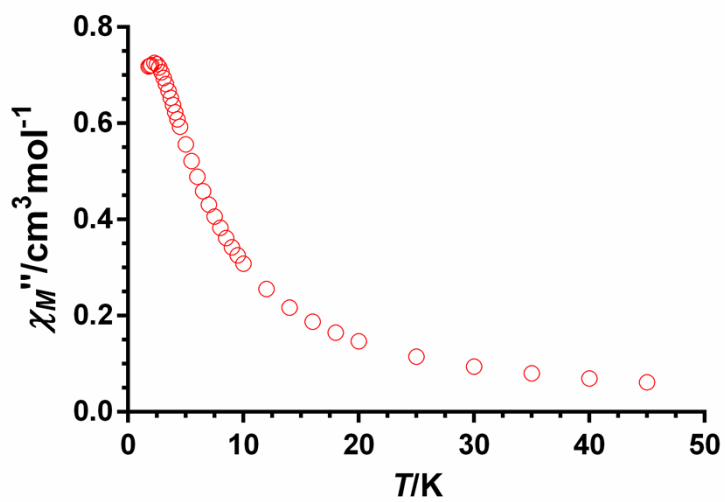


Figure S10. Temperature dependence of the χ_M for **2**.

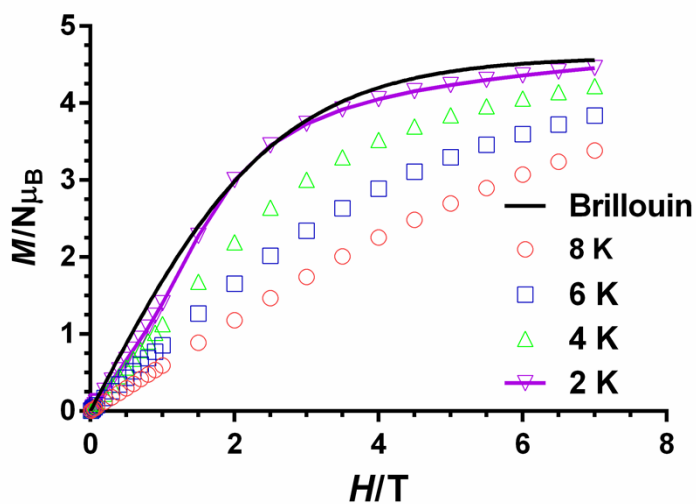


Figure S11. Field dependence of the magnetization for **1** at different temperatures (2–8 K). The solid black line represent the Brillouin function curve for four non-interacting $S = 1/2$ ions with $g = 2.3$. The solid violet line is only a guide for the eyes to highlights its sigmoidal shape.

Table S2. Bond Valence Calculation of **1**

	R	R0	(R0-R)/B	$S_{ij} = \exp\{(R0-R)/B\}$
Fe1–C1	1.920(4)	1.689	-0.624	0.54
Fe1–C2	1.921(5)	1.689	-0.627	0.53
Fe1–C3	1.922(5)	1.689	-0.629	0.53
Fe1–N8	1.960(4)	1.70	-0.703	0.49
Fe1–N10	1.966(3)	1.70	-0.719	0.48
Fe1–N12	1.985(3)	1.70	-0.770	0.46
			V	3.03
Mn1–O1	2.386(3)	1.790	-1.611	0.20
Mn1–N1	2.236(3)	1.84	-1.070	0.34
Mn1–N4	2.200(4)	1.84	-0.973	0.38
Mn1–N6	2.369(4)	1.84	-1.430	0.24
Mn1–N7	2.231(4)	1.84	-1.057	0.35
Mn1–Cl1	2.3642(13)	2.133	-0.625	0.53
			V	2.04

Crystallographic data

Table S3. Data Collection and Structure Refinement Parameters for $[\text{Fe}^{\text{III}}(\text{Tp})(\text{CN})_2(\mu\text{-CN})\text{Mn}^{\text{II}}\text{Cl}(\text{HL}^1)]\cdot 3\text{DMF}$ (**1**) and $\{[\text{Fe}^{\text{III}}(\text{Tp})(\text{CN})(\mu_2\text{-NC})_2\text{Cu}^{\text{II}}(\text{HL}^2)](\text{ClO}_4)\}_2\cdot 6\text{DMF}$ (**2**).

	1	2
Empirical formula	$\text{BC}_{43}\text{ClFeH}_{53}\text{MnN}_{16}\text{O}_4$	$\text{B}_2\text{C}_{88}\text{Cl}_2\text{Cu}_2\text{Fe}_2\text{H}_{104}\text{N}_{30}\text{O}_{16}$
Formula weight	1015.06	2169.31
Temperature/K	100	100
Crystal system	triclinic	triclinic
Space group	P-1	P-1
$a/\text{\AA}$	9.3138(6)	12.1562(14)
$b/\text{\AA}$	16.1466(11)	14.2336(16)
$c/\text{\AA}$	16.5173(10)	15.5600(18)
α/deg	104.669(2)	95.765(4)
β/deg	93.059(2)	105.730(4)
γ/deg	101.198(2)	108.664(3)
Volume/ \AA^3	2343.5(3)	2402.9(5)
Z	2	1
$\rho_{\text{calc}}/\text{g/cm}^3$	1.439	1.499
μ/mm^{-1}	0.697	0.870
F(000)	1056.0	1124.0
Crystal size/ mm^3	$0.1 \times 0.06 \times 0.05$	$0.2 \times 0.1 \times 0.05$
Radiation	MoK α ($\lambda = 0.71073$)	MoK α ($\lambda = 0.71073$)
2 θ range for data collection/ $^\circ$	5.266 to 56.476	5.42 to 56.834
Index ranges	$-12 \leq h \leq 12, -21 \leq k \leq 21, -21 \leq l \leq 21$	$-16 \leq h \leq 16, -19 \leq k \leq 19, -20 \leq l \leq 20$
Reflections collected	33873	52360
Independent reflections	11551 [$R_{\text{int}} = 0.1684, R_{\text{sigma}} = 0.1857$]	12004 [$R_{\text{int}} = 0.0667, R_{\text{sigma}} = 0.0584$]

Data/restraints/parameters	11551/3/568	12004/0/557
Goodness-of-fit on F ²	1.002	1.096
Final R indexes [I] ≥ 2σ (I)]	R ₁ = 0.0748, wR ₂ = 0.1563	R ₁ = 0.0637, wR ₂ = 0.1319
Final R indexes [all data]	R ₁ = 0.1448, wR ₂ = 0.1925	R ₁ = 0.0834, wR ₂ = 0.1409
Largest diff. peak/hole / e Å ⁻³	0.66/-0.88	0.50/-0.64

$${}^a R_1 = \Sigma(|F_o| - |F_c|) / \Sigma |F_o|. \quad {}^b wR_2 = \{\Sigma[w(|F_o|^2 - |F_c|^2)^2] / \Sigma[w(|F_o|^2)^2]\}^{1/2}$$

DFT study

Table S4. Energies (B3LYP/TZVP) of the calculated monomers.

Complex	Species	Charge ^a	Multiplicity	Energy/Hartree
1	Fe(III)	-1	2	-2244.9317820
			6	-2244.8218776
	Fe(II)	-2	1	-2244.8894625
			5	-2244.7653156
	Mn(II) ^b	0	6	-3098.6016142
			2	-3098.5057645
	Mn(III) ^b	+1	5	-3098.3682159
			3	-3098.3228478
2	Fe(III)	-1	2	-2244.9317820

			6	-2244.8218776
--	--	--	---	---------------

^a Charge of the whole monomer considered. ^b An additional DMF molecule interacting with the monomer by hydrogen bonding has also been included in the calculation.

It could be drawn that the most stable pair for complex **1** is that of Fe(III-LS)-Mn(II-HS), and that Fe(III-LS) is the most stable configuration for iron in complex **2**.

Spin densities

As appear in Figure S12, the singly occupied molecular orbital (SOMO), or magnetic orbital, in the iron(III) center of complex **1** is the d_{xy} , represented by the spin density map presented on the left of the figure, which is orthogonal to the magnetic orbitals of manganese(II) ion, represented by the spin density contour presented on the right. This is the basis of the ferromagnetism calculated for this compound. It could be pointed out that Mn(II) ion mainly delocalizes through a σ direct exchange mechanism, whereas the Fe(III) center exhibits a polarization mechanism, with alternating positive and negative spin density values. This could be related with the noteworthy back bonding process on the iron(III), which has a spin density greater than one electron, see Table S3, whereas manganese(II) has a spin density lower than five electrons. The spin density plot of complex **1**, Figure S12, nicely illustrates all these aspects, whereas Table S3 provides selected spin density values for this complex.

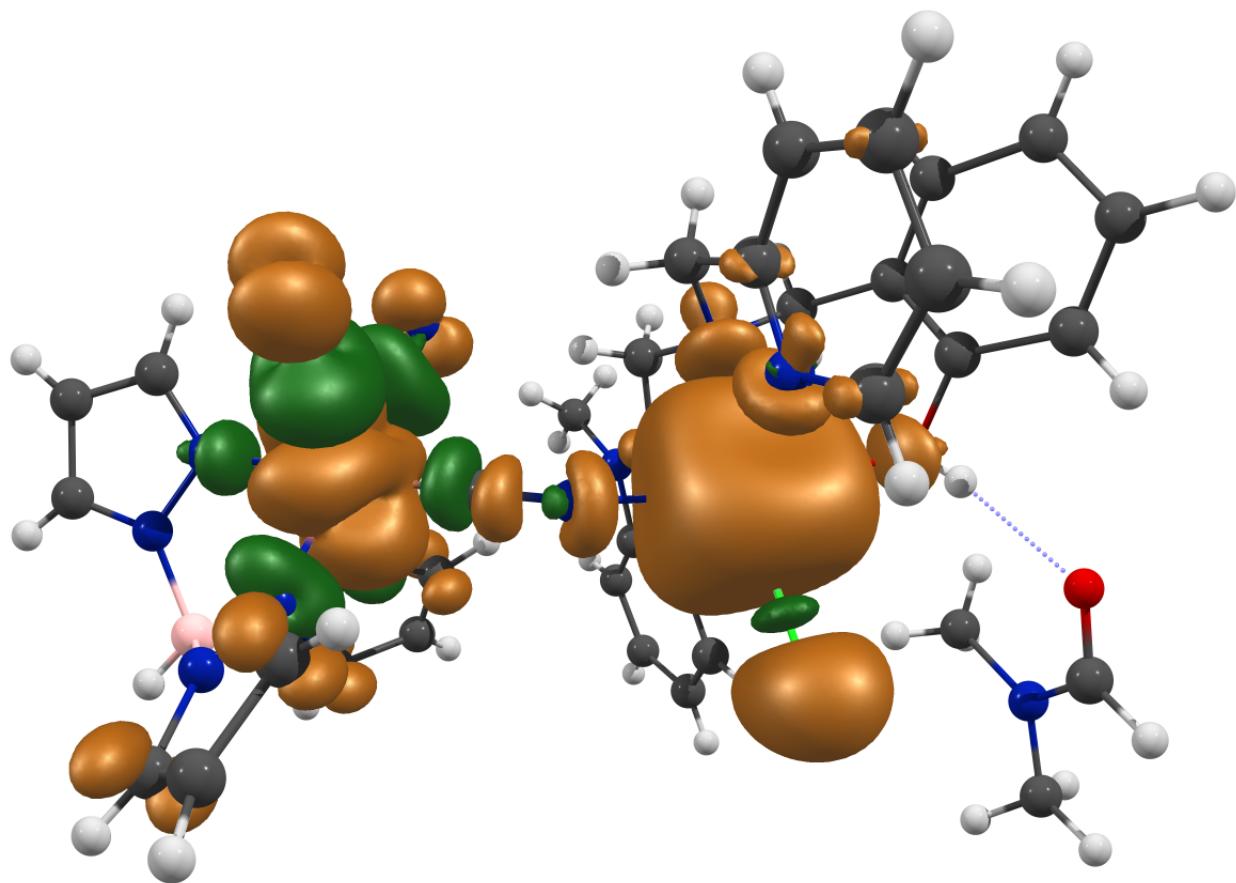


Figure S12. Calculated LC- ω PBE/TZVP spin density for the broken-symmetry septuplet state (parallel, ++, spin configuration) of **1**. Orange and green surfaces indicate positive and negative spin densities, respectively (cut-off at $0.001 e \cdot \text{Bohr}^{-3}$).

Table S5. LC- ω PBE and B3LYP/TZVP spin density values (in electrons) on selected atoms for complex **1**.

Complex 1	LC- ω PBE	B3LYP
Mn	+4.9087	+4.8261
Cl	+0.0429	+0.0716
N _{imi} ^a	-0.0094	-0.0010
N _{ami} ^a	+0.0026	+0.0077

N _{pyr} ^a	-0.0135	-0.0031
N _{cya} ^a	-0.0620	-0.0023
O(H)	-0.0020	-0.0006
Fe	+1.1267	+1.0901
N _{pyra} ^b	-0.0295 (mean)	-0.0208 (mean)
C _{cya} ^c	-0.0731 (mean)	-0.0637 (mean)
C _{cya} ^d	-0.0137	-0.0123

^aRespectively for coordinated nitrogens of imidazole, amine, pyrimidine and cyanide bridge ligands. ^bMean values of the three nitrogen atoms of pyrazole ligands. ^cMean values of the two carbon atoms of single cyanide ligands. ^dCarbon atom of the cyanide bridge ligand.

The spin density plot of complex **2** is shown in Figure S13. Note that the spin density of the copper atom is in the $d_{x^2-y^2}$ orbital, which is orthogonal to the mixed d_{yz}/d_{zx} orbitals in Fe,¹⁷ and that copper ion highly delocalizes through a σ direct exchange leading to a spin density much lower than one electron, whereas iron ion receives an excess of electron density thanks to the back bonding process. As an example, the LC- ω PBE spin density on copper atoms is +0.6243, whereas for iron atoms is +1.1332 electrons.

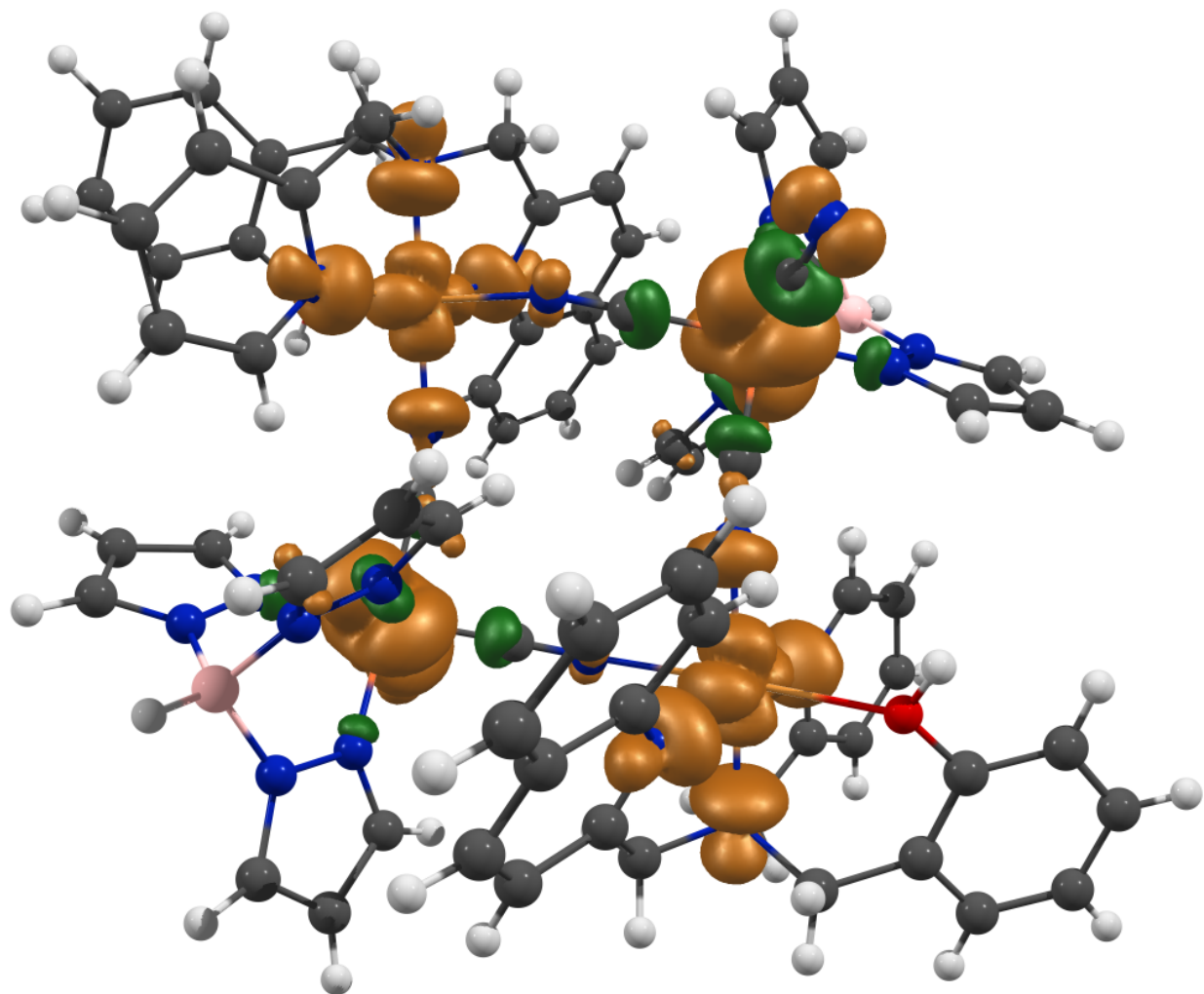


Figure S13. Calculated LC- ω PBE/TZVP spin density for the broken-symmetry quintuplet state (parallel, + + + +, spin configuration) of **2**. Orange and green surfaces indicate positive and negative spin densities, respectively (cut-off at $0.001 e \cdot \text{Bohr}^{-3}$).